

Quantitative Model of Electrochemical Ostwald Ripening and Its Application to the Time-Dependent Electrode Potential of Nanocrystalline Metals

A. Schröder,[†] J. Fleig,^{‡,*} D. Gryaznov,[†] J. Maier,^{*,†} and W. Sitte[§]

Max-Planck-Institut für Festkörperforschung, Heisenbergstr. 1, 70569 Stuttgart, Germany, Vienna University of Technology, Institute of Chemical Technologies and Analytics, Getreidemarkt 9/164EC, 1060 Vienna, Austria, and Montanuniversität Leoben, Institut für Physikalische Chemie, Franz-Josef-Strasse 18, A-8700 Leoben, Austria

Received: February 7, 2006; In Final Form: April 20, 2006

The contact of a metastable nanocrystalline metal ensemble with a metal ion electrolyte leads to an electrochemical Ostwald ripening. The kinetics is modeled on the level of irreversible thermodynamics for the case that the rate is controlled by the electrode/electrolyte transfer resistance. In particular, the kinetic behavior of medium-sized particles and the time dependence of the electromotive force is investigated. Even though it is expressed in electrochemical terms (mixed potential), the modeling is also applicable to chemical Ostwald ripening as long as it is interfacially controlled. Under these conditions, the kinetics exhibits, even though not self-accelerating, strong similarities to selection dynamics, with the competition stemming from the cannibalistic nature of the process.

Introduction

One characteristic feature of nanocrystalline materials is that their thermodynamic properties differ from those of the corresponding macrocrystalline materials. Measurements of the electrical open circuit potential of electrochemical cells (emf, E) afford direct access to precise and reliable thermodynamic data, and have been applied successfully to a variety of examples.^{1–8} Cells composed of nanocrystalline metal electrodes and a macrocrystalline metal reference electrode separated by a metal ion conductor yield, to a first approximation, the size-related excess emf, E^{ex} , and thus the excess chemical potential of the small metal particle, μ^{ex} , according to

$$E^{\text{ex}} = \frac{\mu^{\text{ex}}}{zF} = \frac{V_m 2\gamma}{zFr} \quad (1)$$

where z is the charge number of the ions, F is Faraday's constant, V_m is the molar volume of the investigated compound, γ is the interfacial tension, and r is the particle radius. A closer look into the thermodynamics^{9,10} shows that the situation is more subtle even if we ignore the influence of edges and corners (we also assume γ not to depend on r). One point refers to the deviation from the Wulff shape, that is, to practically important situations in which γ/r is not independent of the crystallographic direction. In such cases we conceive γ and r only as mean values. An even more important point refers to the metastability of the arrangement that we face if we refer to a durable nanocrystalline morphology.⁶ Clearly in the case of elemental crystals such as nanocrystalline silver, this implies a nonzero gradient of the chemical potential of silver (and hence of the electrochemical potential of Ag^+) within the nanocrystalline arrangement. A consequence of this point is that μ^{ex} and hence

γ and r in eq 1 have to be related to the direct contact of Ag with the electrolyte. Figure 1a depicts a cell with a single nanocrystalline particle, which is expected to develop an emf given by eq 1.

While these points are addressed elsewhere,^{6–8} in this paper we will concentrate on a kinetic phenomenon, namely on the inherent instability of the cell even at temperatures under which the isolated nanocrystalline metal phase is durable. Note that for an evaluable emf to be established, there must be a fast exchange of electrons between the particles (direct contact or indirect via current collector), a fast metal ion exchange between the metal particles and the electrolyte (holds for particles in contact with the ion conductor), as well as a rapid ion flux in the electrolyte. These are, however, exactly the conditions that allow for an electrochemically based Ostwald^{6,19,20} ripening of the nanocrystalline particles. Even under open circuit conditions, where the outer current is zero, ions are exchanged laterally between the particles via the electrolyte, and a parallel electronic current runs through the metal particles and/or the metallic current collector (Figure 1b). Therefore, an intrinsic instability results in the case of nanocrystalline metals in contact with an electrolyte where the corresponding ion is mobile. In other words, the sluggish metal ion transport within the nanocrystalline material itself, which prevents the arrangement from undergoing conventional Ostwald ripening, is replaced by a rapid metal ion transport through the electrolyte. This leads to a grain growth by a mechanism that has been termed electrochemical Ostwald ripening¹⁹ and thus to a time-dependent emf.

In this context let us make the following remarks: (i) As mentioned already, only particles with an interface to the electrolyte and with an electronic contact to the current collector contribute to the measurable emf; it is exactly these particles that are subject to lateral growth by electrochemical Ostwald ripening (see above). (ii) In electrochemical terms, the lateral processes (electron conduction in the electrode and ion conduction in the electrolyte) constitute a mixed potential.^{11,12} (iii) Because a size fluctuation leads to an amplification of the

* Corresponding author. E-mail: s.weiglein@fkf.mpg.de.

[†] Max-Planck-Institut für Festkörperforschung.

[‡] Vienna University of Technology.

[§] Montanuniversität Leoben, Institut für Physikalische Chemie.

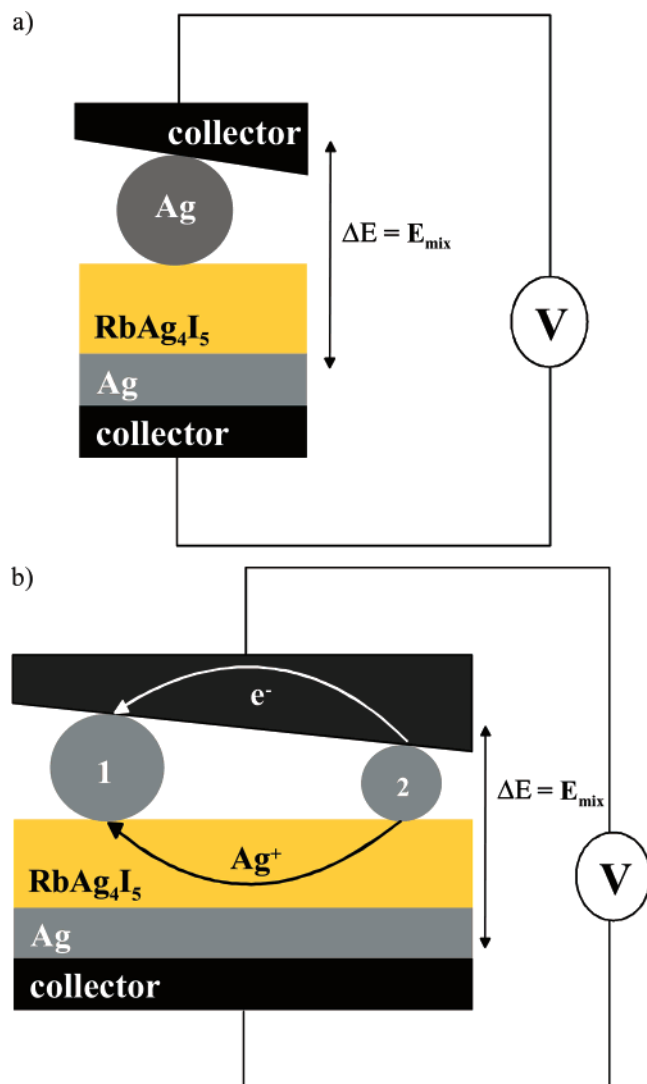


Figure 1. (a) Schematic electrochemical cell in which the working electrode consists of a single nanocrystalline particle ($r = r_1$). The cell voltage corresponds to exactly the excess emf of the particle of radius r_1 , according to eq 1. (b) Scheme of electrochemical Ostwald ripening for two particles. The larger particle (1) grows at the cost of the smaller one (2). The potential difference between the nanocrystalline working electrode (top) and the macrocrystalline reference electrode (bottom) can be measured by an electrometer.

driving force, the inherent instability of the nanocrystalline metal contact with an electrolyte also applies to an initially uniform nanocrystalline arrangement. In other words, if the size difference between a slightly larger particle and a slightly smaller particle is termed L ($L = L_{\text{Japunov}}$ function), then it holds that $L \cdot L' > 0$ guarantees instability in principle¹³ until a single crystal has formed. Although the final stages and also the alterations distant from the electrolyte interface may be extremely sluggish, the variation of the nanocrystalline arrangement close to the interface (which dominates the emf) should be observable.

The basic equations governing Ostwald ripening of precipitates in solution as well as analytical calculations on the corresponding time dependencies have been presented by Wagner in ref 14. However, unlike treatments of transport and reaction-controlled chemical Ostwald ripening,^{14–18} only a few contributions on electrochemical Ostwald ripening are available in the literature: The model for electrochemical Ostwald ripening by Mulder and Sluyters¹⁹ describes two Hg droplets on a platinum electrode that are immersed in an aqueous Hg electrolyte. The model is not directly generalizable to more

particles (see below). Redmond et al.²⁰ present the reforming of silver films when exposed to liquid silver electrolytes and qualitatively mention the analogy to the mixed potential of corrosion.

In this contribution, we present a quantitative model that is able to calculate the emf of a nanocrystalline material with different grain sizes and simulates the time-dependence of the particle sizes and thus the emf variation caused by electrochemical Ostwald ripening.

Even though we will refer to a full electrochemical cell, it is obvious that a half-cell suffices for the phenomena to be observed. Moreover, the results are also applicable to chemical Ostwald ripening, if interfacially controlled. (We will return to this point at the end.) However, it is clear that whenever the electrochemical mechanism is not important, the equations have to coincide with those in ref 14 for the reaction-limited process.

Model

Even though electrochemical Ostwald ripening involves only the metal–electrolyte contact, that is, the half cell Ag (nano) | electrolyte, we consider a full electrochemical cell that consists of nanocrystalline silver as the working electrode and macrocrystalline silver (r so large that the Gibbs–Kelvin term is negligible) as the reference electrode. Then the chemical potential directly relates to a well-defined measurable cell voltage, E .

Even under open circuit conditions a nonzero lateral current will flow corresponding to the rate of the growth process. Even though the transfer resistance of Ag^+ from the metal particles at the contact to the electrolyte has to be sufficiently rapid for a meaningful emf to be observed, it is, and certainly can be assumed in most cases, to be the most sluggish step in the process of electrochemical Ostwald ripening as experimentally shown for the system Ag/RbAg₄I₅ in ref 6. Hence, the area specific resistance \tilde{R}_{el} of the Ag^+ transfer resistance determines the current. For the case of simplicity, we consider only small deviations from equilibrium and thus a linear I – E relation according to

$$I_i = \frac{(E - E_i^{\text{ex}})A_i}{\tilde{R}_{\text{el}}} \quad (2)$$

I_i is the current flowing into particle i , and A_i denotes the contact area of the particle to the electrolyte. A rigorous proof of eq 2 is given in the Appendix. E_i^{ex} is proportional to the excess chemical potential of the silver particle of the size category i and hence represents the emf that a durable monomodal distribution of i particles would develop if located directly at the interface to the electrolyte (since only there does a reaction between electrons and ions takes place). The current, I_i , and hence the growth rate can also be expressed as being proportional to the difference in the excess chemical potentials of particle i and its mean value averaged over cell particles. This formulation is preferred if one refers to interfacially controlled chemical Ostwald ripening.

Figure 2a shows the linearized current–voltage diagram of two differently sized particles (Figure 1b), where $r_1 > r_2$. Because the slope of the I – E curve is proportional to the contact area (eq 2), not only different E_i^{ex} but also different slopes result for the two particles. In an electrode consisting of two particles of different size (Figure 1b), however, the high concentration and mobility of electrons enforces a constant electrochemical potential of the electrons, and thus an effective emf rather than two different E_i^{ex} values result. This effective

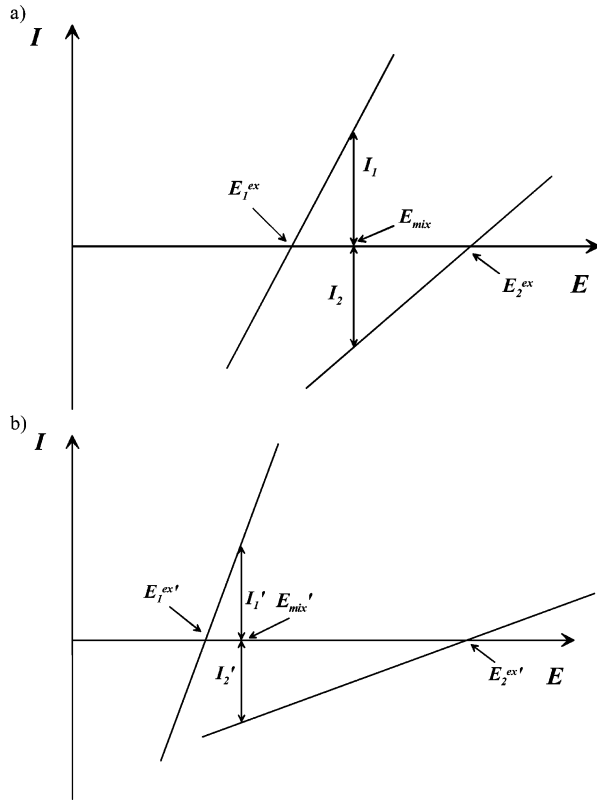


Figure 2. Linearized current–voltage diagrams of two silver particles without direct physical contact with each other, but in simultaneous electronic and ionic contact. (a) The initial situation, (b) the situation after some “Ostwald ripening” ($I_1 = -I_2$).

emf is obviously a mixed potential: Without an external current (open circuit) the emf is given by a E_{mix} value lying between E_2^{ex} and E_1^{ex} such that the individual currents of the particles cancel ($I_1 = -I_2$). Owing to this internal current, I_i , the smaller particle becomes smaller, and the larger one becomes larger. The slope of the larger particle thus becomes even steeper (larger area), and that of the smaller one even shallower (smaller area); moreover, E_2^{ex} shifts to larger values, and E_1^{ex} shifts to lower values. This is sketched in Figure 2b.

In the following, this model is quantified and solved numerically. According to eq 2, the current flow into a particle i is given by

$$I_i = \frac{(E_{\text{mix}} - E_i^{\text{ex}})A_i}{\tilde{R}_{\text{el}}} = \frac{(E_{\text{mix}} - E_i^{\text{ex}})r_i^2 f}{\tilde{R}_{\text{el}}} \quad (3)$$

The area factor, f , depends on how much the electrode particle is pressed into the electrolyte. A contact area of πr_i^2 has been used in these calculations. From eq 3, valid for particles 1 and 2, $I_1 = -I_2$ (mass balance), $z = 1$ for Ag ions and eq 1 we obtain

$$E_{\text{mix}} = \frac{E_1^{\text{ex}}A_1 + E_2^{\text{ex}}A_2}{A_1 + A_2} = \frac{E_1^{\text{ex}}r_1^2 + E_2^{\text{ex}}r_2^2}{r_1^2 + r_2^2} = \frac{2\gamma V_m}{F} \frac{r_1 + r_2}{r_1^2 + r_2^2} \quad (4)$$

Hence, $I_1 (= -I_2)$ can also be written as

$$I_1 = \frac{1}{\tilde{R}_{\text{el}}/A_1 + \tilde{R}_{\text{el}}/A_2} (E_2^{\text{ex}} - E_1^{\text{ex}}) = \frac{2f\gamma V_m}{(r_1^{-2} + r_2^{-2})F\tilde{R}_{\text{el}}} \left(\frac{1}{r_2} - \frac{1}{r_1} \right) \quad (5)$$

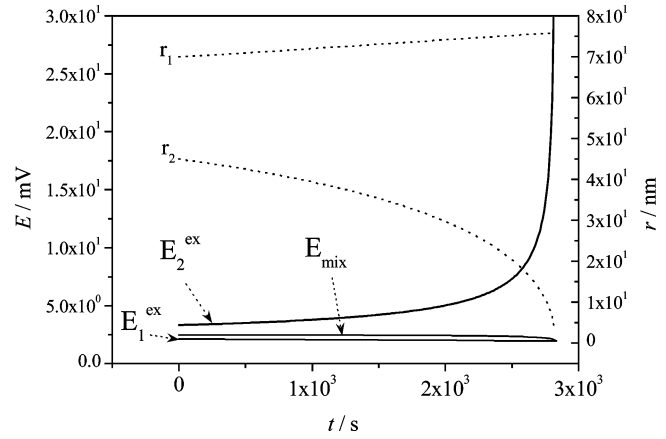


Figure 3. Time-dependent potentials (solid curves) and radii (dotted curves) for a nanocrystalline electrode consisting of two particles ($r_1 = 70$ nm, $r_2 = 45$ nm).

Equation 5 can be interpreted as the current generated by the growth driving force ($E_2^{\text{ex}} - E_1^{\text{ex}}$) limited by the sum of the two transfer resistances ($R_1 + R_2 = \tilde{R}_{\text{el}}/A_1 + \tilde{R}_{\text{el}}/A_2$).

The internal current, I_1 , corresponds to matter transport from one particle to the other and thus leads to time-dependent particle sizes and a time-dependent emf. This is modeled numerically as follows: The charge, Q_i , transferred by Ag^+ ions corresponds to a volume (V_i) change of the corresponding particles according to

$$I_i = \frac{dQ_i}{dt} = \frac{dV_i}{dt} \frac{F}{V_m} \quad (6)$$

Hence, by using eq 5

$$\frac{dV_1}{dt} = \frac{2f\gamma V_m (r_2^{-1} - r_1^{-1})}{F^2 \tilde{R}_{\text{el}} (r_1^{-2} + r_2^{-2})} \quad (7)$$

results. For numerical calculations, this is transformed to the corresponding difference equation solved iteratively. The iteration in the numerical calculation is set to stop when the radius reaches the value of 0.3 nm (corresponding to a cluster of four Ag atoms) or when the particle volume becomes formally negative. At this point, the contribution of the smallest particle(s) to the emf is usually less than 1%. Figure 3 shows the calculated values of the particle radii and the various potentials versus time. As also sketched in Figure 2b, E_{mix} is closer to the potential of the larger particle, E_1^{ex} .

Owing to electrochemical Ostwald ripening, the smaller particle becomes even smaller and its excess emf E_i^{ex} increases sharply, especially just before it vanishes completely. Nevertheless, the closer E_{mix} is to the potential of the larger particle, the larger the difference in size because a small area fraction decreases the influence of a particle (cf. eq 4). Yet, the small particles have an increased influence on E_{mix} if there are many of them as will be discussed in more detail below.

Figure 4a shows the situation after the introduction of a third particle. Accordingly, the interplay of three electrochemical reactions (one at each particle) determine the measured emf. It is shown in the Appendix that eq 3 is still correct whereby E_{mix} has to be generalized as

$$E_{\text{mix}} = \frac{\sum_k E_k^{\text{ex}} A_k}{\sum_k A_k} = \frac{\sum_k E_k^{\text{ex}} r_k^2}{\sum_k r_k^2} = \frac{2\gamma V_m}{F} \frac{\sum_k r_k}{\sum_k r_k^2} \quad (8)$$

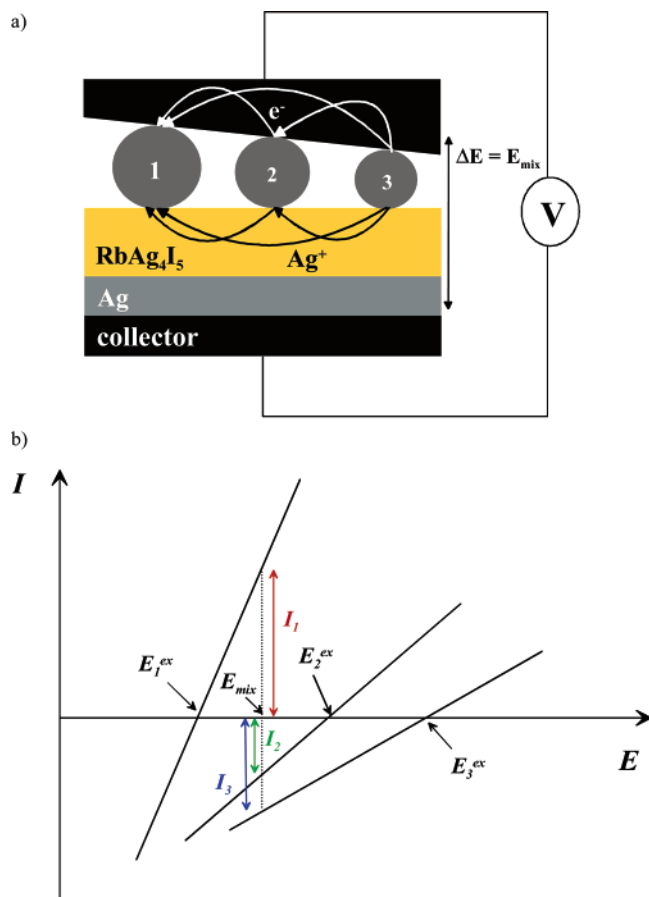


Figure 4. Scheme of electrochemical Ostwald ripening for three particles (a) and linearized current–voltage diagrams of three silver particles, $\Sigma I_i = 0$ (b).

However, the flux, I_i , can now no longer be conceived as a particle-to-particle flux driven by the respective E_i values (cf. eq 5). (Variations of V_m with particle size are neglected.) The linearized I – E characteristics leading to the mixed potential, E_{mix} , are sketched in Figure 4b. From eqs 3 and 6 we obtain

$$\frac{dV_i}{dt} = \frac{(E_{\text{mix}} - E_i^{\text{ex}}) f r_i^2 V_m}{F \tilde{R}_{\text{el}}} \quad (9)$$

Owing to $dV_i/dt = 4\pi r_i^2 dr_i/dt$, eq 9 yields with eq 1

$$\frac{dr_i}{dt} = \left(E_{\text{mix}} - \frac{2\gamma V_m}{F r_i} \right) \frac{f V_m}{4\pi F \tilde{R}_{\text{el}}} = \left(\frac{\sum_k r_k}{\sum_k r_k^2} - \frac{1}{r_i} \right) \frac{\gamma f V_m^2}{2\pi F^2 \tilde{R}_{\text{el}}} \quad (10)$$

and the corresponding difference equation again makes possible a simple numerical calculation of the time-dependent grain size and emf. Equation 10 is analogous to eq V.8 in ref 14 derived for Ostwald ripening of precipitates in solution with the mixed potential replacing the effective concentration as a measurable quantity.

An interesting question concerning the three-particle arrangement is how the middle-sized sphere behaves, whether it shrinks or grows, that is, whether the parallel electronic and ionic currents from the small particle to the medium or those from the medium to the large particle dominate. Figure 5 exemplarily shows the behavior of a system with particle radii of 70, 55, and 45 nm: not only the small but also the middle particle shrinks right from the beginning. For particle sizes of 70, 55, and 15 nm as well as of 10 μm , 55 nm, and 45 nm (Figure 6),

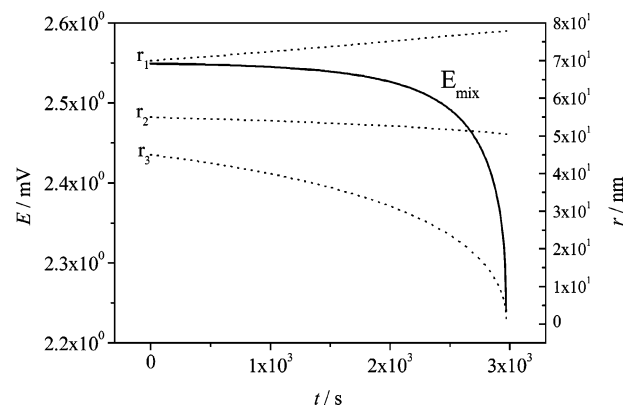


Figure 5. Time-dependent potential (solid curve) and radii (dotted curves) for a nanocrystalline electrode consisting of three particles ($r_1 = 70$ nm, $r_2 = 55$ nm, $r_3 = 45$ nm).

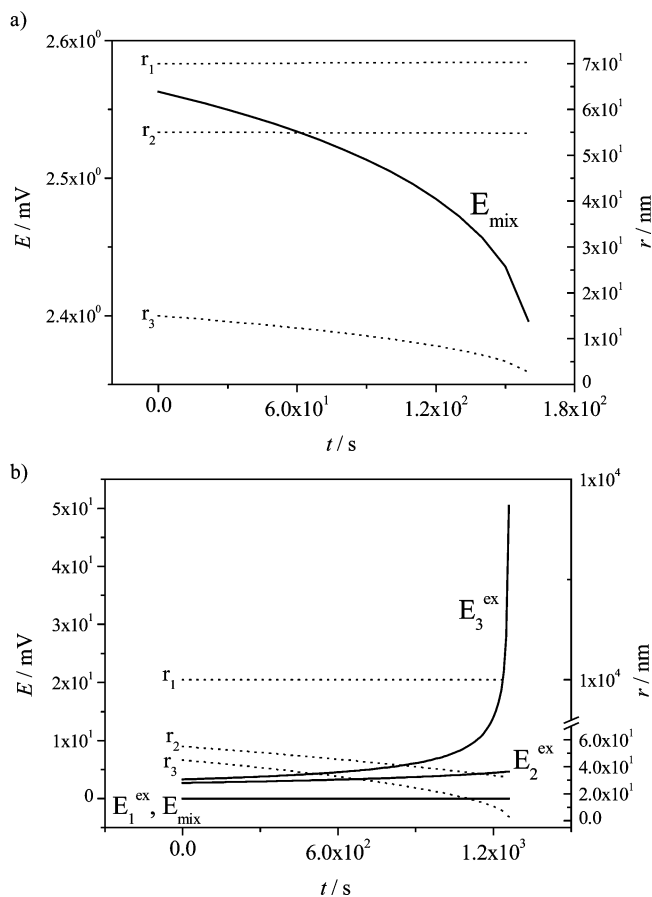


Figure 6. Time evolution of potentials (solid curves) and radii (dotted curves) for a nanocrystalline electrode consisting of three particles (a) $r_1 = 70$ nm, $r_2 = 55$ nm, $r_3 = 15$ nm, (b) $r_1 = 10$ μm , $r_2 = 55$ nm, $r_3 = 45$ nm.

again both the medium and the small particle shrink steadily. In the latter case, E_{mix} is almost equivalent to the potential of the large particle and has a very low value (which is to be expected because of the small surface contributions). From eqs 8 and 9, however, it can be calculated easily that for $r_2 > (r_1^2 + r_3^2)/(r_1 + r_3)$ not only the large but also the medium-sized particle grows. Please note that the assumption of the interfacial process to be rate determining makes the calculations independent of the particle positions.

As has been mentioned above, an interesting variation of the model is achieved when the differently sized individual particles are replaced by size categories k with different amounts of

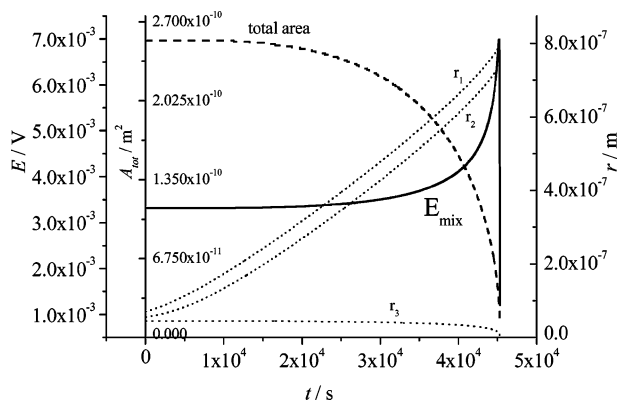


Figure 7. Evolution of potential (solid curve) and radii (dotted curves) for a nanocrystalline electrode consisting of 1 large, 1 medium, and 10 000 small particles ($r_1 = 70$ nm, $r_2 = 55$ nm, $r_3 = 45$ nm). Additionally, the evolution of the total area (dashed curve) is shown.

particles in each size category. Even though eq 3 no longer describes the particle-to-particle current, eq 8 is still valid with the area now being the total area of the corresponding category with n_k particles of contact area A_k (each) and hence

$$E_{\text{mix}} = \frac{\sum_k E_k^{\text{ex}} n_k A_k}{\sum_k n_k A_k} \quad (11)$$

results.

As an example, Figure 7 shows the result for 10^4 particles of $r_3 = 45$ nm, one of $r_2 = 55$ nm, and one of $r_1 = 70$ nm, that is, the radii also used in Figure 5. The initial E_{mix} value is significantly higher for many particles (3.3 mV compared to 2.5 mV for three particles). More surprising, however, is the fact that E_{mix} rises before it decays rapidly. This is due to the different proportionalities of $E_k^{\text{ex}} \propto r_k^{-1}$ and $A_k \propto r_k^2$ and shows that E_{mix} is not a reversible emf because the total area (also shown in Figure 7), and consequently the free enthalpy, sinks steadily. Hereafter, the total area, A_{tot} , was calculated as a sum of the surface areas of spherical particles for each size category, that is, $\sum_k 4\pi n_k r_k^2$. Furthermore, the electrochemical Ostwald ripening takes more time for this system, namely 10^4 s instead of 10^3 s, and the middle particle starts growing, while it shrinks steadily in Figure 5. Figure 8 shows simulations with the same values for the radii, but different numbers of particles. In Figure 8a, there are 10^4 small and 18 medium particles, respectively, and 1 large particle. The initial E_{mix} value starts at 3.4 mV and increases less before it decreases, reflecting the reduced area fraction of small particles (although the absolute area of the small particles stays the same). E_{mix} again rises and decays steeply toward the end. Figure 8b shows the results for 10^4 small and medium particles and 1 large particle. The E_{mix} curve starts at about 2.95 mV and decays steadily.

It is possible to numerically calculate the parameter range for which E_{mix} first rises before it decreases. (See Figure 9, which refers to a system with one large particle, of radius 100 nm, and a large number of small particles of identical size r .)

To draw a realistic picture of a more homogeneous size distribution, we introduced nine size categories, with numbers reflecting the real size distribution of nanocrystalline silver investigated in refs 6 and 7. Figure 10 shows the size distribution and the simulation of E_{mix} for the respective initial values of the radii as well as the evolution of all nine radii with time until the smallest size category is so small that it is set to disappear (as mentioned above, these smallest particles contribute only less than 1% to the E_{mix} at this stage). The

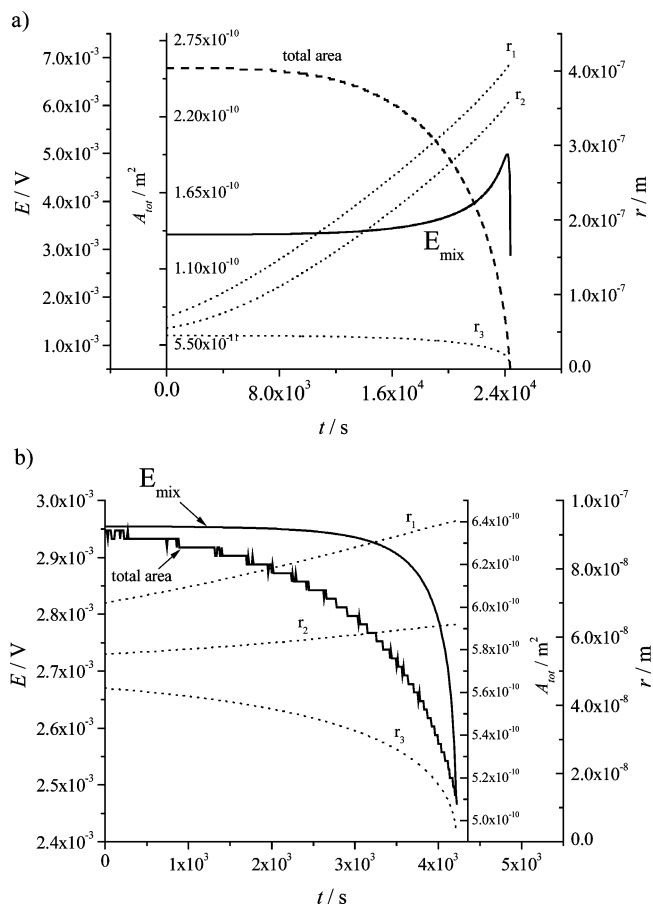


Figure 8. (a) Evolution of potentials (solid curves) and radii (dotted curves) for a nanocrystalline electrode consisting of 1 large, 18 medium, and 10 000 small particles, (b) 1 large, 10 000 medium, and 10 000 small particles. The initial radii are the same as those in Figure 7. Additionally, the evolution of the total area (solid curve, should be distinguished from E_{mix}) for both cases is shown.

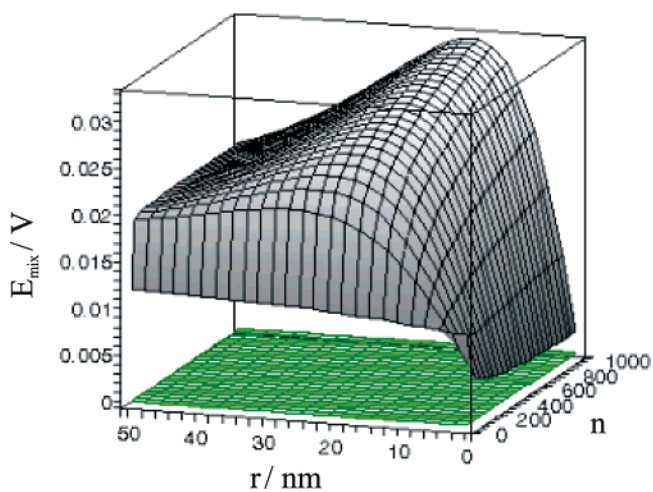


Figure 9. Three-dimensional diagram of E_{mix} vs particle number n and particle radius r of the small particles, for a constant radius of the single large particle (100 nm) (two size categories).

simulation is then continued for the eight remaining size categories. Their respective values from the end of the first simulation become the initial values of the new simulation. The process is repeated until only the largest size category remains. Figure 11 summarizes the results for all of these consecutive simulations, showing E_{mix} and the radii as a function of time. The striking agreement with experiment is addressed in the next section.

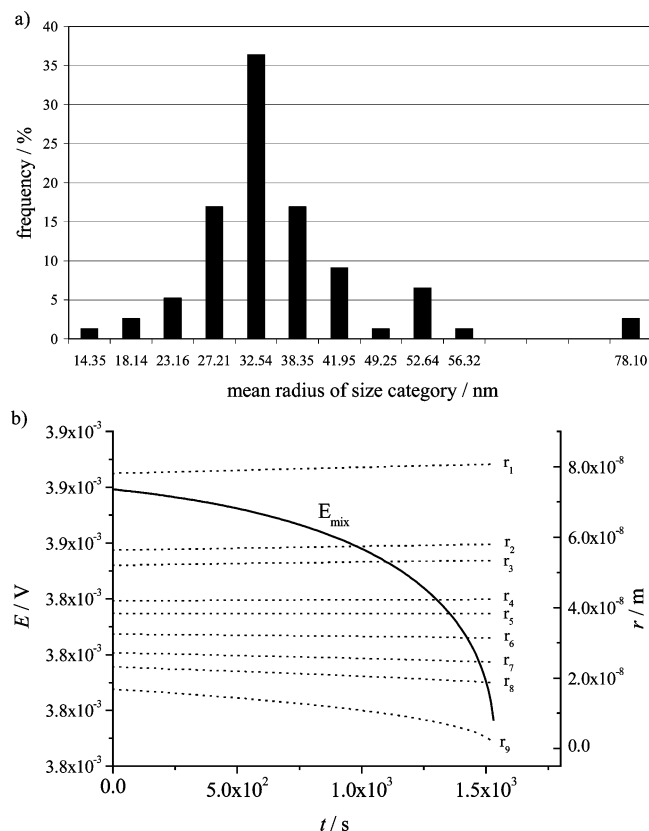


Figure 10. (a) Real size distribution of a nanocrystalline silver particle, as determined from TEM images. (b) E_{mix} (solid curve) and the radii (dotted curves) of the nine size categories as a function of time until the smallest particles have diminished.

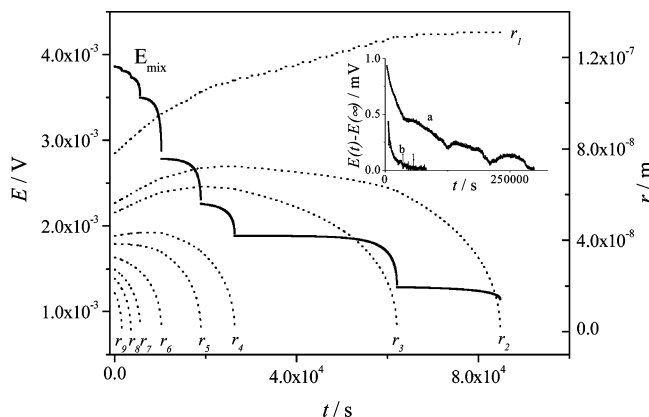


Figure 11. Consecutive simulation of E_{mix} (solid curve) and the radii (dotted curves) of the nine size categories as a function of time. Below a certain radius, the respective smallest category disappears and the simulation continues with the respective larger size categories. The inset shows (a) experimental results of a nano-Ag sample, which approximately shows an exponential decay as obtained for a simulation of a continuous size distribution. The roughness is due to temperature fluctuations. The relaxation time is $\sim 10^5$ s. The inset also shows (b) experimental results for roughened silver exhibiting a time constant of $\sim 10^4$ s.

Remarkably, the individual E_{mix} curves show a positive curvature, while the overall E_{mix} curvature is negative and can roughly be approximated with an exponential decay. This observation is reasonable because the size differences become smaller and the mean radii become larger, which causes the initially steep decay to become increasingly shallow in the course of simulation, and the absolute value of E_{mix} approaches zero. This exponential decay is also quantifiable and comparable

to experiments (the inset of Figure 11 shows a typical experiment; a detailed discussion of experimental results is given in ref 7). Using parameter values of the Ag/RbAg₄I₅ system from literature (γ) and our own experiments (R_{el}),^{6,7} the time constant amounts to 10^4 s. Values obtained experimentally^{6,7} for nanocrystalline Ag are typically larger by an order of magnitude (see Figure 11, inset a), which seems tolerable in view of the complexity of the real system. Because literature values taken for γ refer to free surfaces, the estimated time constant has to be taken as an upper limit. (Emf values refer to contacted surfaces. Note that the grain boundary tension is smaller by almost 1 order of magnitude. The inset also shows a relaxation curve (b) for roughened silver with similar feature sizes but with a time constant matching the estimated values better.) Comparing the activation energies is more reliable: From simulations performed for different temperatures (using the respective electrode resistances), one calculates an activation energy of 0.009 eV, which is in fair agreement with the experimental value (0.013 ± 0.005 eV).

Interfacially Controlled Ostwald Ripening as Cannibalistic Selection Kinetics

The aforementioned treatment, which was given in terms of cell potentials, should not conceal the fact that the electrochemical process refers to the contact of the metal with the electrolyte and its occurrence does not require a complete electrochemical cell. If just a minimum phase arrangement is to be considered, then one perhaps better refers (see eq 9) to chemical potentials instead of cell potentials, the interconnection given by eqs 1 and 11. This notion then also allows a more straightforward application to chemical interfacially controlled Ostwald ripening. As in interfacially controlled processes, the positional coordinate is unimportant and the kinetic equations correspond to homogeneous kinetics. It is now interesting to compare the decisive eq 10

$$\frac{\partial r_i}{\partial t} = (W_i^{\text{ex}}(r_i) - W_{\text{mix}}) \quad (12)$$

with the result for homogeneous parallel competition reactions, describing how several species, i , grow or die while competing about the same resources or due to the constraint of constant population. (Such kinetics were discussed in detail by Eigen,^{21,22} Ebeling, and Feistel;²³ see also Haken.²⁴) In the latter case, the well-known Eigen equation

$$\frac{\partial x_i}{\partial t} = (W_i^{\text{ex}} - \langle W^{\text{ex}} \rangle) x_i \quad (13)$$

results (W_i , excess productivity; $\langle W \rangle$, average excess productivity; x , concentration). For a better comparison, we have introduced in eq 12 symbols for the negative potentials, that is, $W_i^{\text{ex}} \equiv -\text{const} \times E_i^{\text{ex}}$ and $W_{\text{mix}} \equiv -\text{const} \times E_{\text{mix}}$ (the latter being given by eq 8). First of all, one notices a dissimilarity: While eq 13 describes an autocatalytic process, the ripening process described by eq 12 is not autocatalytic because in the latter case the growth probability does not increase statistically with increasing size. (In fact, the simulations always show a sublinear growth, $\partial^2 r / \partial t^2 < 0$, if the number of particles is not too small.) More important, however, is the following striking similarity as far as the destiny of the particles/species is concerned: In both cases the distance of the individual parameter, W_i , to the mean value (W_{mix} or $\langle W^{\text{ex}} \rangle$) decides about the destiny of “ i ”, whether it survives or dies out. Because this

threshold value is an average over the W_i^{ex} values, in the competition game the mean value ("high jump bar"²¹) is rising continuously so that in the end only one species (here the largest crystal) survives. (As can be readily shown, the r -dependence of W_i^{ex} in the case of eq 12 does not destroy the properties that (i) W_{mix} is always between the W values of the smallest and the largest particles and that (ii) W_{mix} increases, if the particles with the smallest W_i^{ex} disappear.) Particles with smaller sizes, even though growing in the beginning, die out eventually. The competition in Ostwald ripening comes from the cannibalistic nature of the process. The distinction between the simplest competition conditions in selection dynamics, viz. limited amount of common resources (total mass conserved) and given total concentration ($\sum I_i = 0$), is no longer meaningful here for the same reason.

Conclusions and Outlook

A quantitative model for electrochemical Ostwald ripening has been introduced. The evolutions of the measurable open circuit potential, E_{mix} , and of the particle radii with time have been simulated. The numerical procedure is able to model the growth mechanism in the case of two, three, or a multitude of differently sized particles. The respective values for the mixed potential, the time constant of relaxation, and its activation energy are in reasonable agreement with previous electrochemical (emf and ac) experiments. The fact that we discussed the kinetics in electrochemical terms should not conceal that the driving force $E_{\text{mix}} - E_i^{\text{ex}}$ represents the negative difference between the individual chemical excess potential and its mean value (area averaged). In this form, the kinetic results are directly applicable to a normal Ostwald ripening provided it is interfacially controlled. The distances between the particles then do not play any role, and the effectively homogeneous kinetics arrived at exhibits qualitative similarities to the selection kinetics as discussed in refs 21–24. In the case of Ostwald ripening, the competition arises intrinsically from the cannibalistic nature of the process (total mass is restricted).

Appendix

Consider Figure 1b. The electrochemical potential of the electron is uniform in the electrode. Regarding the electrochemical potential of the silver ion ($\tilde{\mu}_{\text{Ag}^+}$), it can be considered constant within a single nanocrystalline particle, i , but then drops to a different constant value in the electrolyte (transfer limitation). Because there is no external (macroscopic) current flow, there are no gradients in the electrochemical potential of the silver ions in the electrolyte or of the electrons ($\tilde{\mu}_{e^-}$) within an electrode. The emf E between the top and bottom electrode can be written as $(\tilde{\mu}_{e^-}(\text{top}) - \tilde{\mu}_{e^-}(\text{bottom}))/F$, and hence $EF = \tilde{\mu}_{e^-}(\text{top}) + \tilde{\mu}_{\text{Ag}^+}(\text{bottom}) - \mu_{\text{Ag}}^{\circ}(\text{bottom})$ or

$$E = [\tilde{\mu}_{e^-}(\text{top}) + \tilde{\mu}_{\text{Ag}^+}(\text{electrolyte}) - \mu_{\text{Ag}}^{\circ}]/F \quad (\text{A1})$$

results. Symbol μ_{Ag}° denotes the chemical potential of bulk silver. The local Ag^+ current, I_i , out of a silver particle i into the electrolyte (or vice versa) is given by

$$I_i = \frac{A_i}{\bar{R}_{\text{el}}F}(\tilde{\mu}_{\text{Ag}^+}(\text{electrolyte}) - \tilde{\mu}_{\text{Ag}^+}(i)) = \frac{A_i}{\bar{R}_{\text{el}}F}(\tilde{\mu}_{\text{Ag}^+}(\text{electrolyte}) - \mu_{\text{Ag}}(i) + \tilde{\mu}_{e^-}(\text{top})) = \frac{A_i}{\bar{R}_{\text{el}}F}(\tilde{\mu}_{\text{Ag}^+}(\text{electrolyte}) - \mu_{\text{Ag}}^{\circ} - \mu_{\text{Ag}}^{\text{ex}}(i) + \tilde{\mu}_{e^-}(\text{top})) \quad (\text{A2})$$

where the excess term is $\mu_{\text{Ag}}^{\text{ex}}(i) = \mu_{\text{Ag}}(i) - \mu_{\text{Ag}}^{\circ} = 2\bar{\gamma}_i V_m/r_i$; \bar{R}_{el} is assumed to be invariant. Combination of eqs A1 and A2 leads to

$$I_i = \frac{A_i}{\bar{R}_{\text{el}}} (E - E_i^{\text{ex}}) \quad (\text{A3})$$

where $E_i^{\text{ex}} \equiv \mu_{\text{Ag}}^{\text{ex}}(i)/F$. E_i^{ex} thus refers to the cell voltage if only a single particle of radii r_i were present. While the charge balance demands locally $I_{\text{Ag}^+} = -I_{e^-}$, mass balance requires

$$\sum_k I_k = 0 \quad (\text{A4})$$

under open circuit conductions. Using eqs A3 and A4 it follows for E_{mix}

$$E = E_{\text{mix}} \equiv \frac{\sum_i A_i E_i^{\text{ex}}}{\sum_i A_i} \quad (\text{A5})$$

Equation A5 reveals the mixed potential nature of the emf.

References and Notes

- (1) Plieth, W. J. *J. Phys. Chem.* **1982**, *86*, 3166.
- (2) Gärtner, F.; Bormann, R.; Birringer, R.; Tschöpe, A. *Scr. Mater.* **1996**, *35*, 805.
- (3) Villain, S.; Cabané, J.; Knauth, P. *Scr. Mater.* **1997**, *38*, 1003.
- (4) Gräf, Ch. P.; Heim, U.; Schwitzgebel, G. *Solid State Ionics* **2000**, *131*, 165.
- (5) Villain, S.; Knauth, P.; Schwitzgebel, G. *J. Phys. Chem. B* **1997**, *101*, 7452.
- (6) Schroeder, A.; Fleig, J.; Drings, H.; Wuerschum, R.; Maier, J.; Sitte, W. *Solid State Ionics* **2004**, *173*, 95.
- (7) (a) Schröder, A.; Fleig, J.; Maier, J.; Sitte, W. *Electrochim. Acta*, in press. (b) Schröder, A. Ph.D. Thesis, University of Leoben, Austria, 2005.
- (8) Schröder, A.; Fleig, J.; Maier, J.; Sitte, W., to be submitted for publication.
- (9) Defay, R.; Prigogine, I.; Bellemans, A.; Everett, H. *Surface Tension and Adsorption*; John Wiley & Sons: Ltd.: New York, 1960.
- (10) Rusanov, A. I. *Phasengleichgewichte und Grenzflächenerscheinungen*; Akademie-Verlag: Berlin, 1978.
- (11) Wagner, C.; Traud, W. *Z. Elektrochem.* **1938**, *44*, 391.
- (12) Lange, E. Z. *Elektrochem.* **1951**, *55*, 76.
- (13) (a) Hahn, W. *The Stability of Motion*; Springer-Verlag: Berlin, 1967. (b) Pontryagin, L. S. *Ordinary Differential Equations*; Addison-Wesley: Reading, MA, 1962.
- (14) Wagner, C. Z. *Elektrochem.* **1961**, *65*, 581.
- (15) Hayashi, K.; Matsuoka, N. *J. Adv. Mater.* **2002**, *34*, 38.
- (16) Matsuoka, N.; Hayashi, K. *Processing and Fabrication of Advanced Materials VI*; IOM Communications: London, 1998; p 35.
- (17) Yao, J. H.; Elder, K. R.; Guo, H.; Grant, M. *Phys. Rev. B* **1993**, *47*, 14110–25.
- (18) Lifshitz, I. M.; Slyozov, V. V. *J. Phys. Chem. Solids* **1961**, *19*, 35.
- (19) Mulder, W. H.; Sluyters, J. H. J. *Electroanal. Chem.* **1999**, *468*, 127.
- (20) Redmond, P. L.; Hallock, A. J.; Brus, L. E. *Nano Lett.* **2005**, *5*, 131.
- (21) Eigen, M. *Naturwissenschaften* **1971**, *58*, 465.
- (22) Küppers, B. *Molecular Theory of Evaluation*; Springer-Verlag: Berlin, 1983.
- (23) Ebeling, W.; Feistel, R. *Physik der Selbstorganisation und Evolution*; Akademie-Verlag: Berlin, 1982.
- (24) Haken, H. *Synergetik*; Springer-Verlag: Berlin, 1990.